Journal of Materials Chemistry

Cite this: *J. Mater. Chem.*, 2011, **21**, 3952

www.rsc.org/materials

PAPER

Electrical and dielectric properties of polyaniline–Al_2O_3 nanocomposites derived from various Al_2O_3 nanostructures

Jiahua Zhu,[a] Suying Wei,[b] Lei Zhang,[a] Yuanbing Mao,[c] Jongeun Ryu,[d] Neel Haldolaarachchige,[e] David P. Young[e] and Zhanhu Guo*[a]

Received 12th November 2010, Accepted 4th January 2011
DOI: 10.1039/c0jm03908j

Four Al_2O_3 nanostructures (*i.e.* nanofiber, nanoplatelet, nanorod and nanoflake) have been successfully synthesized *via* hydrothermal procedures followed by a dehydration process. Subsequently, polyaniline (PANI) nanocomposites incorporating these four Al_2O_3 nanostructures have been fabricated using a surface initialized polymerization (SIP) method. Both TEM and SEM are used to characterize the morphologies of the Al_2O_3 nanostructures and PANI/Al_2O_3 nanocomposites. X-Ray diffraction results reveal that the morphology of the nanofiller has a significant effect on the crystallization behavior of the PANI during polymerization. The electrical conductivity and dielectric permittivity of these nanocomposites are strongly related to both the morphology of the filler and the dispersion quality. Temperature-dependent-conductivity measurements from 50–290 K show that the electron transportation of the nanocomposites follows a quasi 3-d variable range hopping (VRH) conduction mechanism. The extent of charge carrier delocalization calculated from VRH is well correlated to the dielectric response of these nanocomposites. Thermogravimetric analysis (TGA) and differential scanning calorimetry (DSC) results reveal an enhanced thermal stability of the PANI/Al_2O_3 nanocomposites as compared to that of pure PANI due to the strong interaction between the nanofillers and polymer matrix. The mechanism of the SIP method is also elaborated in this work.

1. Introduction

Polymer nanocomposites (PNCs) have received tremendous attention due to their striking advantageous properties of polymers such as lightweight, easy processability and flexibility, and the functional characteristics of the nanofillers such as high mechanical strength and excellent electrical, dielectrical, optical and magnetic properties. Therefore, various structural PNCs with different functionalities have been fabricated using advanced technologies, such as ultrastrong multilayer PNCs by layer-by-layer technique[1,2] and magnetic PNC fibers using electrospinning method.[3,4] All these promising properties allow PNCs to be applied in diverse areas such as microwave absorbers,[5,6] electronics,[7,8] sensors[9] and energy storage devices.[10]

Nanomaterials are one kind of materials that have sizes smaller than 100 nm in at least one dimension. Nanotechnology is expanding extensively to various fields of interests due to the novel physical, chemical, and biological properties of nanomaterials. Recent research indicates that the properties of nanomaterials are strongly related to their size and morphology. Xia *et al.* summarize the fabrication, characterization and structure–property relationship on several nanostructures including wires, rods, belts and tubes.[11] The electrical, magnetic and optical properties of nanomaterials can also be size- and shape-dependent. One typical example is quantum dots, where the emission wavelength is able to be tuned through controlling the particle size and morphology.[12,13] Another example is a size- and shape-dependent morphological transformation of nanostructured materials, where titanate nanostructures being transformed into their anatase titania counterparts are demonstrated during a hydrothermal soft chemical process.[14] Specifically, lepidocrocite hydrogen titanate nanotubes with diameters of about 10 nm are transformed into anatase nanoparticles with an average size of 12 nm. Lepidocrocite hydrogen titanate nanowires with relatively small diameters (average diameter range of ≤200 nm) are converted into single-crystalline anatase nanowires with relatively smooth surfaces. Larger diameter (>200 nm) titanate wires are transformed into analogous anatase submicron wire motifs, resembling clusters of adjoining anatase

[a]*Integrated Composites Laboratory (ICL), Dan F. Smith Department of Chemical Engineering, Lamar University, Beaumont, TX, 77710, USA. E-mail: zhanhu.guo@lamar.edu; Tel: +1 (409) 880-7654*
[b]*Department of Chemistry and Biochemistry, Lamar University, Beaumont, TX, 77710, USA*
[c]*Department of Chemistry, University of Texas—Pan American, Edinburg, TX, 78539, USA*
[d]*Department of Mechanical & Aerospace Engineering, University of California Los Angeles, Los Angeles, CA, 90095, USA*
[e]*Department of Physics and Astronomy, Louisiana State University, Baton Rouge, Louisiana, 70803, USA*

nanocrystals with perfectly parallel, oriented fringes. In addition, the structural difference of nanomaterials provides them with preferential capabilities in specific applications. For example, WO_3 nanorods[15] and mesoporous WO_3[16] find their applications in electrochromic devices, while WO_3 nanoparticles,[17] nanofibers[18] and hollow spheres[19] show excellent performances as gas sensors to detect acetone, ammonia and alcohol, respectively. Recently, "metacomposites" with negative permittivity including polypyrrole/WO_3[20] and polyaniline/WO_3[21] PNCs are successfully fabricated using a surface initialized polymerization (SIP) method in our group.

Polyaniline (PANI) is unique among the conjugated polymers since its conductivity can be readily controlled through doping/dedoping process. Nanostructured PANI provides the possibility of the enhanced performance due to its high specific surface area.[22,23] However, it is still difficult to fabricate PANI with different nanostructures through a simple chemical process. Al_2O_3 has been extensively studied to serve as catalysts, absorbents, fire retardants and fillers for structural materials.[24–27] Al_2O_3 nanostructures are easier to produce through a hydrothermal process, more important, Al_2O_3 is stable in the acidic and oxidative environments while polymerizing aniline, together with the low cost, Al_2O_3 could be a competitive candidate as "seed" to fabricate different nanostructured PANI/Al_2O_3 PNCs targeting at different physiochemical properties. However, electrical and dielectric properties of conductive PNCs reinforced with Al_2O_3 have been rarely reported, especially stemmed from Al_2O_3 nanostructures with various morphologies.

In this work, four different Al_2O_3 nanostructures (*i.e.* nanofiber, nanoplatelet, nanorod and nanoflake) have been synthesized *via* hydrothermal process and their corresponding conductive PANI/Al_2O_3 PNCs have been fabricated using a surface initialized polymerization method. The temperature dependent resistivity and frequency dependent dielectric permittivity are investigated and the results indicate that these properties are strongly related to the morphology and dispersion quality of the Al_2O_3 fillers. The thermal properties of the PANI/Al_2O_3 PNCs are improved compared to that of pure PANI, as investigated by thermogravimetric analysis (TGA) and differential scanning calorimetry (DSC).

2. Experimental

2.1. Materials

Aniline (C_6H_7N), ammonium persulfate (APS, $(NH_4)_2S_2O_8$), and *p*-toluene sulfonic acid (PTSA, $C_7H_8O_3S$) are purchased from Sigma Aldrich. Aluminium nitrate, ammonia, aluminium isopropoxide ($Al(OC_3H_7)_3$, 98+%), and hydrazine monohydrate ($N_2H_4 \cdot H_2O$) are purchased from Alfa Aesar. All the chemicals are used as-received without any further treatment.

2.2. Synthesis of four Al_2O_3 nanostructures

Al_2O_3 nanofiber (NFB). First, boehmite nanofibers were produced using a literature reported method.[28] Briefly, aluminium nitrate (0.02 mole) was dissolved in ultra-pure water (12.6 ml). Then 10 wt% ammonia aqueous solution was added dropwise into the above solution while stirring vigorously until pH reaches 5. The mixture was stirred at room temperature for one hour. The obtained gel was filtrated and the residue was transferred into a 25 ml glass beaker. Before putting the beaker into a Teflon vessel (125 ml), 2 ml ultrapure water was poured to the bottom of the Teflon vessel. The Teflon vessel was then sealed and heated at 170 °C for 3 days. The resulting material was washed several times with ultrapure water, centrifuged, and dried in air at 60 °C for 2 days before calcination.

Al_2O_3 nanoplatelet (NPT). As reported previously,[29] boehmite nanoplatelets had been synthesized as follows: aluminium isopropoxide (0.5 mol) was added to distilled water (50 ml) followed by vigorously stirring for one hour at 80 °C. Subsequently, the mixture was poured into a 125 ml Teflon vessel. The vessel was sealed and heated for 24 hours at 200 °C and then allowed to cool down to room temperature. The suspension was filtered and washed with distilled water for several times before γ-AlOOH nanoplatelets were obtained. Subsequently, the sample was dried in an oven at 60 °C before calcination.

Al_2O_3 nanorod (NRD). A hydrothermal method was employed to synthesize boehmite nanorods.[30] Typically, aluminium nitrate (13 mmol) was dissolved in distilled water (80 ml) to form a transparent solution and hydrazine monohydrate ($N_2H_4 \cdot H_2O$, 45 mmol) was added dropwise into the solution, giving rise to milky precipitates at pH = 5. Subsequently, the mixture was poured into a 125 ml Teflon vessel. The vessel was sealed and placed in an oven for 12 hours at 200 °C. The resultant colloidal product was filtered, washed with distilled water and absolute ethanol for several times, and then dried under vacuum at 60 °C for 6 hours before calcination.

Al_2O_3 nanoflake (NFK). The boehmite nanoflakes were fabricated following the same procedure as used for fabricating boehmite nanorods but with different molar ratios of the reactants.[30] Aluminium nitrate (13 mmol) and hydrazine monohydrate ($N_2H_4 \cdot H_2O$, 62 mmol) were involved, and the initial and ultimate pH values of the solution were almost the same (around 10).

After the hydrothermal procedures for boehmite nanostructures, the as-prepared four samples were respectively calcined at 600 °C for 3 hours, resulting in the corresponding four Al_2O_3 nanostructures.

2.3. Fabrication of PANI/Al_2O_3 nanocomposites

Four types of PANI/Al_2O_3 PNCs were fabricated with the same surface initialized polymerization method by introducing the four different Al_2O_3 nanostructures. Initially, an Al_2O_3 nanostructured powder (0.373 g) was mixed with PTSA/APS solution with a fixed ratio of 30 mmol : 18 mmol in 200 ml deionized water, following by one-hour sonication in an ice-water bath. Then an aniline solution (36 mmol in 50 ml deionized water, molar ratio of APS : PTSA : aniline = 3 : 5 : 6) was mixed with the above nano-Al_2O_3 suspension at 0 °C and sonicated for additional one hour in ice-water bath for further polymerization. The product was vacuum filtered and washed with deionized water until the filtrate reached pH = 7. The obtained PANI/Al_2O_3 nanocomposite powders were dried at 50 °C. Pure PANI

was synthesized following the same procedure without adding any Al_2O_3 nanomaterials.

2.4. Characterization

Fourier transform infrared spectroscopy (FT-IR, Bruker Inc. Vector 22, coupled with an ATR accessory) was used to characterize the pure PANI and its Al_2O_3 PNCs in the range of 500 to 4000 cm^{-1} at a resolution of 4 cm^{-1}. FT-IR was also used to determine the nanoparticle surface functionality.

The morphology of the PNCs was characterized with scanning electron microscope (SEM, JEOL field emission scanning electron microscope, JSM-6700F). The nanofillers' morphology, distribution and interaction with PANI were determined by TEM using a Philips CM-200 transmission electron microscope with a LaB_6 filament at an accelerating voltage of 120 kV. Samples for TEM analysis were made from drying a drop of Al_2O_3 nanomaterial or PANI/Al_2O_3 nanocomposite powders suspended in ethanol after a brief sonication for about 30 s on carbon-coated copper TEM grids.

X-Ray diffraction (XRD) analysis was performed on a Bruker D8 Focus diffractometer equipped with a Sol-X detector using a copper radiation source. Data were collected over a 2θ angle range of 10–60° at a resolution of 0.05° per step with a 6 s integration time per step.

Dielectric properties were measured by a LCR meter (Agilent, E4980A) equipped with a dielectric test fixture (Agilent, 16451B) at the frequency of 20 Hz to 2 MHz and at room temperature. Pure PANI and PNC powders were pressed in a form of disc pellets with a diameter of 25 mm by applying a pressure of 95 MPa in a hydraulic presser and the average thickness was about 0.5 mm. The same sample was used to measure the electrical conductivity (σ) by a standard four probe method within the temperature range of 50–290 K. The temperature dependent resistivity was used to investigate the electron transport mechanism in pure PANI and its PNCs.

The thermal degradation of the PNCs was studied using a thermo-gravimetric analysis (TGA, TA instruments TGA Q-500). TGA was conducted on pure PANI and PANI/Al_2O_3 PNCs from 25 to 800 °C with an airflow rate of 60 ml min^{-1} and a heating rate of 10 °C min^{-1}. Differential scanning calorimeter (DSC, TA Instruments Q2000) measurements were carried out under a nitrogen flow rate of approximately 100 ml min^{-1} at a heating rate of 10 °C min^{-1} from 0 to 250 °C.

3. Results and discussion

3.1. TEM of the four Al_2O_3 nanostructures

Al_2O_3 nanostructured materials with four different morphologies are successfully produced and Fig. 1 shows the corresponding TEM microstructures. Fig. 1(a) clearly shows that the Al_2O_3 is fibrous with very long narrow fibers, some exceeding 500 nm in length and with a width of less than 10 nm. The nanoplatelets (Fig. 1(b)) have a particle size varying from 20 to 80 nm. Fig. 1(c) shows the sample, consisting of a large number of nanorods with a length of less than 200 nm, and Fig. 1(d) demonstrates that the sample is composed of plentiful nanoflakes with sizes of 20–60 nm.

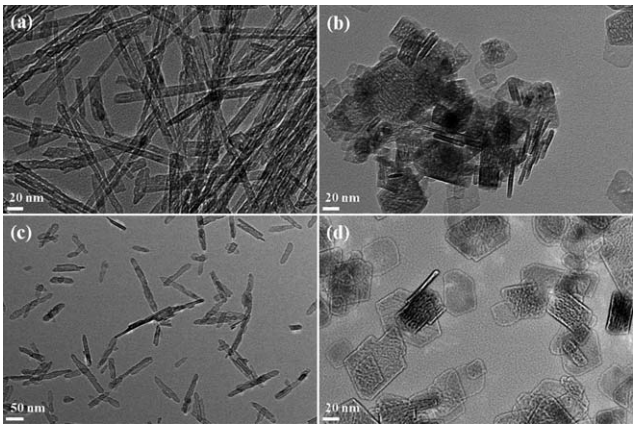

Fig. 1 TEM microstructures of four Al_2O_3 nanostructures: (a) NFB, (b) NPT, (c) NRD and (d) NFK.

3.2. FT-IR analysis

Fig. 2 shows the FT-IR spectra of pure PANI and its PNCs reinforced with different Al_2O_3 nanostructures. The bands at 1566 and 1487 cm^{-1} are assigned to the stretching deformation of quinone and benzene rings of PANI, respectively. The band at 1298 cm^{-1} is attributed to the C–N stretching in a secondary aromatic amine. The peak at 1112 cm^{-1} corresponds to the C–N stretch in quinoid ring. The out-of-plane bending of C–H in the substituted benzene ring is reflected in the 796 cm^{-1} peak. These results are in good agreement with the previous spectroscopic characterization of polyaniline.[31,32] In addition, the PANI/Al_2O_3 PNCs exhibit two absorption bands at 557 cm^{-1} and 528 cm^{-1}, which are attributed to the Al–O stretching vibration.[33] Therefore, it can be concluded that PANI co-exists with inorganic Al_2O_3 nanomaterials in the PANI/Al_2O_3 PNCs on the basis of the FT-IR spectral similarity between the PANI/Al_2O_3 PNCs and the pure PANI as well as the FT-IR spectral features of Al_2O_3.

3.3. XRD analysis

Fig. 3 shows the XRD patterns of pure PANI and its PANI/Al_2O_3 PNCs reinforced with different Al_2O_3 nanostructured fillers. Pure PANI shows two peaks at $2\theta = 19.5°$ and 25.2°, respectively, Fig. 3(a), which correspond to the (100) and (110)

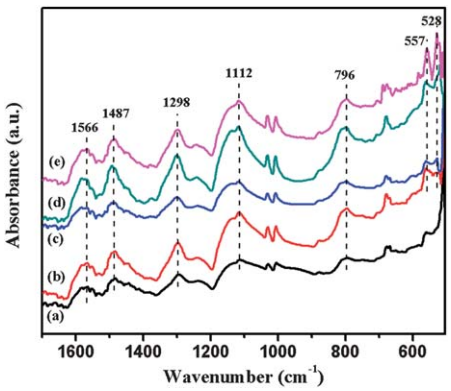

Fig. 2 FT-IR spectra of (a) pure PANI, and PANI PNCs reinforced with (b) NFB, (c) NPT, (d) NRD and (e) NFK, respectively.

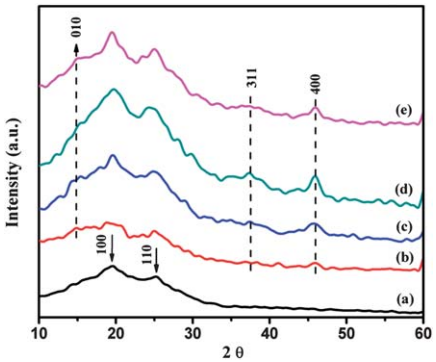

Fig. 3 XRD patterns of (a) pure PANI, and its PNCs reinforced with (b) NFB, (c) NPT, (d) NRD and (e) NFK, respectively.

crystal planes.[34,35] Two additional peaks at $2\theta = 37.4°$ and 45.9° are observed in the PNCs, Fig. 3(b)–(e), which are assigned to (311) and (400) planes of the γ-Al_2O_3.[30] In addition, a new peak of PANI appears at $2\theta = 14.9°$ with a reported (010) plane[34] while the two original peaks ($2\theta = 19.5°$ and 25.2°) are still exhibited in the PNCs, indicating that the nanofillers promote the formation of (010) plane of PANI during the surface initiation polymerization process. However, the slight difference in peak intensity is observed between the pure PANI and the PANI/Al_2O_3 PNCs, Fig. 3(a)–(e). The PNCs reinforced with Al_2O_3 nanofibers show a reduced peak intensity in the positions of $2\theta =$ 19.5° and 25.2° (Fig. 3(b)), while the other PNCs show an increased intensity (Fig. 3(c)–(e)). As previously reported, nanomaterials, including nanotubes,[36] nanofibers[37] and core–shell structure,[38] are able to act as nucleating sites to promote the growth of various nanostructured polymeric composites. A decreased peak intensity of (100) and (110) crystalline planes is observed in the PANI/NFB PNCs (Fig. 3(b)), which is due to the inferior crystallization arising from the internal stress along the nanofiber axis direction during growth. On the contrary, nanofillers with a lower aspect ratio are more favorably serving as "seeds" to initiate the growth of polymers around the nanofillers, which will promote the formation of a defect-free crystalline structure of polymers.[20,39] This is definitely true for the PNCs filled with Al_2O_3 NPT, NRD and NFK in this work.

3.4. SEM and TEM observation of the nanocomposites

Fig. 4 shows the SEM images of the PANI/Al_2O_3 PNCs with 10 wt% different nanostructured Al_2O_3 fillers. Generally, the Al_2O_3 nanomaterials are well dispersed in the PANI matrix except the nanoplatelets, Fig. 4(b). In this case, slight agglomeration and bare polymer matrix are observed as indicated by the white arrows. This observation is consistent with the TEM observation, Fig. 1, confirming that the surface initiated polymerization method is quite efficient to fabricate PNCs from uniformly dispersed nanofillers. However, it is not able to completely separate the agglomerated nanoplatelets during polymerization. Fig. 5 shows the TEM micrographs of the PNCs. The nanofiber surface in PNCs (Fig. 5(a)) becomes rougher as compared to that of pure nanofibers (Fig. 1(a)), which is due to the polymerization occurred on the nanofiber surface and a strong interfacial interaction between the nanofiller and the polymer matrix.

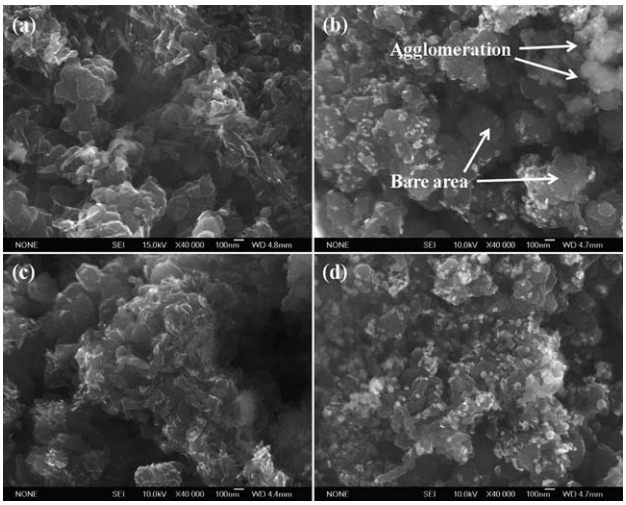

Fig. 4 SEM microstructures of the PANI/Al_2O_3 PNCs reinforced with (a) NFB, (b) NPT, (c) NRD and (d) NFK, respectively.

Similar results are observed in the other PNCs. The agglomeration of nanoplatelets is clearly observed, Fig. 5(b), while the nanorods are well separated and completely wrapped with PANI, Fig. 5(c). The nanoflakes are well dispersed and most of them are presented in the form of an individual flake with the existence of few double-flake stack together, Fig. 5(d).

3.5. Electrical conductivity and electron transport mechanism

Fig. 6(a) shows the resistivity as a function of temperature for pure PANI and its PNCs with 10 wt% different Al_2O_3 nanostructures, respectively. Generally, the resistivity decreases with increasing temperature, indicating a semiconducting behavior of pure PANI and the PNCs in the measured temperature scale.[40] The graph clearly shows that the PNCs exhibit either enhanced (PANI/NPT) or reduced resistivity (PANI/NFB and PANI/NFK) as compared to that of pure PANI. However, it is interesting to find that a junction at ~165 K is observed between the resistivity curves of pure PANI and PANI/NRD. Compared to PANI, a decreased resistivity at lower temperature (75–165 K) and an enhanced resistivity at relatively higher temperature from 165 to 290 K are shown in PANI/NRD. The two dimensional

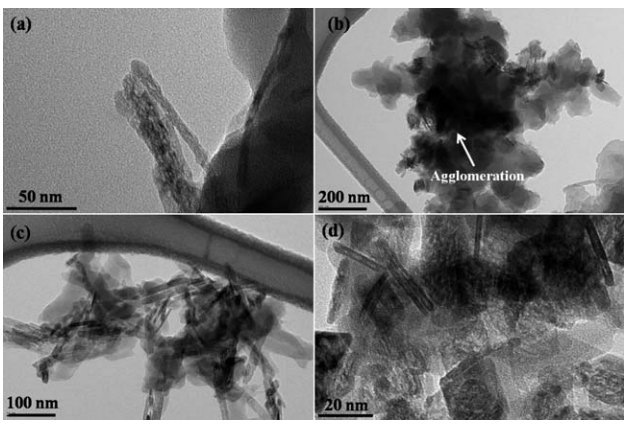

Fig. 5 TEM microstructures of the PANI/Al_2O_3 PNCs reinforced with (a) NFB, (b) NPT, (c) NRD and (d) NFK, respectively.

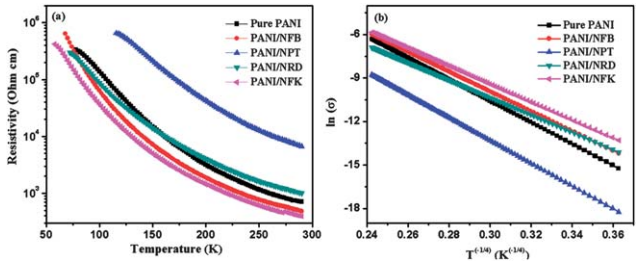

Fig. 6 (a) Resistivity *vs.* temperature and (b) ln (σ)–$T^{(-1/4)}$ curves of pure PANI and PANI/Al_2O_3 PNCs.

nanoflakes, *i.e.* NPT and NFK, seem more promising in decreasing the resistivity than the one-dimensional nanofibers, even though both of these two nanofillers contribute to a decreased resistivity in the PNCs. However, it is interesting to observe that the PANI/NPT PNCs exhibit the highest resistivity among all these samples and show an opposite conduction phenomenon as compared to that of PANI/NFK PNCs, even though the morphologies of these two nanofillers are similar. The major difference of the resistivity in these two PNCs (PANI/NFK and PANI/NPT) may come from the exfoliation degrees of the nanofillers, which are clearly observed in the TEM images of the Al_2O_3 nanostructures (Fig. 1(b) and (d)) and the SEM images of the PANI/NPT and PANI/NFK PNCs (Fig. 4(b) and (d)). The Al_2O_3 nanoplatelets appear to be agglomerated both before (Fig. 1(b)) and after (Fig. 4(b)) the polymerization process, which introduces structural defects and blocks the electron transportation within the PNCs, and finally an enhanced resistivity is observed.

The electron transportation mechanism is investigated through constructing a relation between ln (σ) and $T^{-1/n}$ for each sample, where $n = 2$, 3, and 4. The best fits (standard deviation 0.01) for each sample are obtained with $n = 4$ in the temperature range of 50–290 K. The linear relation between ln (σ) and $T^{-1/4}$, Fig. 6(b), indicates a quasi 3-d variable range hopping (VRH, the low temperature behavior of the resistivity in strongly disordered systems where the states are localized).[41] The temperature dependent VRH conductivity is given by eqn (1)

$$\sigma = \sigma_0 \exp\left[-(T_0/T)^{1/n}\right] \quad (1)$$

where T_0 is the characteristic Mott temperature related to the electronic wave function localization degree and σ_0 is the conductivity at high temperature limit. Generally, a larger T_0 implies a stronger localization of the charge carriers, while small T_0 implies a weak localization.[42] The T_0 and σ_0 for each sample are summarized in Table 1. The experimental results are in good agreement with the theoretical expectations. T_0 increases from 3.02×10^7 K (pure PANI) to 3.82×10^7 K (PANI/NPT), indicating an enhanced localization of the charge carriers, and thus an enhanced resistivity. However, T_0 decreases significantly to 2.17×10^7 K and 1.46×10^7 K for PANI/NFB and PANI/NFK PNCs, respectively, accompanying with the decreased resistivity within the whole temperature range. The decreased resistivity of these PNCs is probably due to the long fiber length of NFB and large surface area of NFK, which are favorable to reduce the contact resistance after coating with conductive PANI. The lowest T_0 and σ_0 are obtained in the PANI/NRD PNCs, reflected in the smallest curve slope, Fig. 6(b).

3.6. Dielectric properties

Fig. 7(a) and (b) show the real permittivity (ε') and dielectric loss (tan δ, where $\tan\delta = \varepsilon''/\varepsilon'$) as a function of the frequency for pure PANI and its PNCs with different Al_2O_3 nanostructures at room temperature. It is interesting to observe that ε' of pure PANI experiences three different stages towards high frequency, which include the increase in the range of 20–10^3 Hz, almost stable within 10^3 to 2×10^4 Hz and then decrease in the frequency range of 2×10^4 to 2×10^6 Hz, while the PNCs only show a monotonically decreased ε' with increasing frequency. The PANI/NPT obtains the highest ε' of 547 at 100 Hz and meanwhile exhibits the sharpest decrease in ε' towards high frequency. The large ε' originates from the Maxwell–Wagner–Sillars effect, in which the charge carriers are accumulated at the internal interfaces.[43] The increased charge carrier localization is verified by the enhanced T_0, Table 1. The decrease of the ε' with increasing frequency is induced by the well known dielectric relaxation phenomena,[44] which suggests that the charge carrier localization is not stable and easily affected by the external frequency disturbances. However, ε' is relatively stable within the whole frequency range for the other PNCs, and the magnitude of ε' follows the sequence: PANI/NRD > PANI/NFB > PANI/NFK. The resistivity variation of all these composites is in the reverse sequence. Generally, higher σ often derives from the easier and faster electron (charge carriers) transportation within the PNCs and thus the electrons tend to move between the two electrodes rather than to stay in a specific location, which leads to the lower ε'.

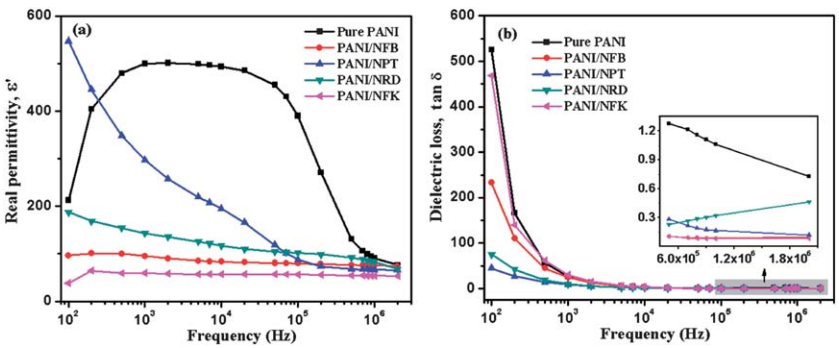

Fig. 7 (a) Real permittivity and (b) dielectric loss as a function of frequency for the pure PANI and PANI/Al_2O_3 PNCs.

Table 1 T_0 and σ_0 for pure PANI and its PNCs

Samples	$T_0 \times 10^7$/K	σ_0/S cm^{-1}
Pure PANI	3.02	115 151
PANI/NFB	2.17	37 835
PANI/NPT	3.82	28 739
PANI/NRD	1.29	2061
PANI/NFK	1.46	9189

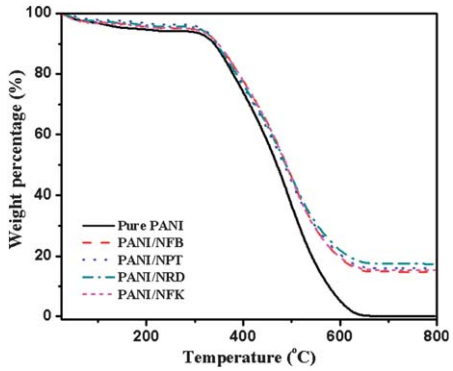

Fig. 8 TGA curves of pure PANI and PANI/Al_2O_3 PNCs.

Fig. 7(b) shows the frequency dependent dielectric loss (tan δ). tan δ decreases significantly within the frequency range from 10^2 to 10^4 Hz and is almost stable at a small value from 10^4 to 10^6 Hz. The inset of Fig. 7(b) depicts tan δ within the frequency of 5×10^5 to 2×10^6 Hz. Similar tan δ curve is observed for PANI/NFB and PANI/NFK PNCs, which exhibit the most stable and lowest tan δ at around 0.1, followed by PANI/NPT and PANI/NRD PNCs. Pure PANI obtains the highest tan δ within the whole frequency range.

3.7. Thermogravimetric analysis

Fig. 8 shows the thermal stability of pure PANI and its PANI/Al_2O_3 PNCs, respectively. All the samples show two distinct weight loss stages. The first stage, which corresponds to 5–7% weight loss from 25 to 250 °C, is due to the evaporation of moisture and solvent residue in the samples. The major weight loss at above 310 °C is attributed to the degradation of PANI. With the addition of the various structured nanofillers, the degradation temperature (10% weight loss of PANI and 11.2% weight loss of PNCs are taken; the additional 1.2% weight loss is calculated from the Al_2O_3 residue (~15%, Fig. 8) times the weight loss of Al_2O_3 itself (~8%, Fig. 11) after thermal degradation) is increased by 14.6, 9.1, 10.3 and 13.8 °C for PANI/NFB, PANI/NPT, PANI/NRD and PANI/NFK PNCs, respectively, as compared to that of pure PANI (340.6 °C). The increased thermal stability is due to a strong interaction between the filler and matrix, which is also observed in PANI/montmorillonite PNCs,[45,46] PANI/Ag PNCs[47] and Fe_3O_4/PANI core/shell structure.[48] It is interesting to observe that the PNCs reinforced with NFB and NFK show better thermal stability than that of the PNCs filled with NRD and NPT. This observation is consistent with the variation of σ in the PNCs, where the former two nanofillers increase σ and the latter two do not (Fig. 6). PANI is completely decomposed in the air at high temperatures (>600 °C). From the TGA analysis, Al_2O_3 in the PNCs is estimated to be 14.7, 16.0, 17.4 and 15.4 wt% for PANI/NFB, PANI/NPT, PANI/NRD and PANI/NFK, respectively. The PNCs have a weight residue much larger than that of the initial particle loading estimation, calculated from the initial weight of particles and monomers. This is due to the incomplete conversion of the aniline monomers to PANI. The slight difference of the residue among the four PNCs arises from the shape effect of the nanofillers on the polymerization.

3.8. Differential scanning calorimetry

DSC measurement is able to provide further information on the thermal property of pure PANI and its PANI/Al_2O_3 PNCs. As shown in Fig. 9, all the samples exhibit a broad endothermic peak below 175 °C (marked with arrows), which is related to the release of moisture and other combined small molecules.[21] This observation is consistent with the slight weight loss in TGA (Fig. 8). Pure PANI is observed to exhibit a small peak around 170 °C while all the different Al_2O_3 nanostructures show a similar small peak at about 150 °C. However, only one peak is observed in the PNCs at relatively higher temperature as compared to the corresponding pure Al_2O_3 nanostructures, which is primarily due to the strong interfacial interaction between the Al_2O_3 nanofiller and PANI matrix.[49,50] The peak overlapping could be excluded because all the four PNCs show only one peak simultaneously. The peak position of the PNCs (Fig. 9(b)–(e)) shifts to higher temperature as compared to that of the pure nanofillers (Fig. 9(b′)–(e′)). The specific melting enthalpy and temperature values are listed in Table 2. However, they are still lower than those of pure PANI due to the relatively weak interaction between the volatile components and PNCs. We consider a more compact structure (or higher crosslinking) of PANI in the PNCs from this SIP method, which prevents the water molecules penetrating into PANI backbone structure. In addition, the shape of the fillers would impose their effect on the formation of PANI structure, thus the slight difference in the peak position is observed among the four PANI/Al_2O_3 PNCs. In addition, a broad exothermic peak, starting from around 125 °C and ending at about 200 °C (marked with arrows), is observed in the PNCs while the nanofillers show only flat lines. This broad

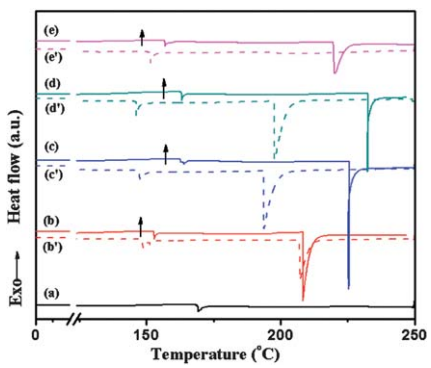

Fig. 9 DSC curves of (a) pure PANI, and its PNCs reinforced with (b) NFB, (c) NPT, (d) NRD and (e) NFK; and pure nanofillers of (b′) NFB, (c′) NPT, (d′) NRD and (e′) NFK. The arrows indicate a broad exothermic peak of the PNCs.

Table 2 DSC characteristics of Al_2O_3 and PANI/Al_2O_3 PNCs

No.	Composition	ΔH_1/J g^{-1}	T_1/°C	ΔH_2/J g^{-1}	T_2/°C
(a)	PANI	5.27	169.4	—	—
(b)	PANI/NFB	1.11	153.0	47.64	208.3
(c)	PANI/NPT	1.65	164.1	36.36	225.3
(d)	PANI/NRD	1.86	163.3	29.79	232.4
(e)	PANI/NFK	2.00	157.0	34.38	220.3
(b′)	NFB	7.17	148.8	41.68	207.3
(c′)	NPT	5.88	147.7	44.37	193.8
(d′)	NRD	10.60	146.4	42.49	197.8
(e′)	NFK	10.62	151.4	18.48	209.7

peak is attributed to a series of reactions, including bond scissioning (endothermic) and bond formation (exothermic).[51] The bond scissioning is compensated by the generated heat from the bond formation, thus shows an exothermic peak at around 125–200 °C. The sharp peak at 200–250 °C is from the Al_2O_3 nanofillers. The large shift of these peaks to higher temperatures indicates a strong interaction between the Al_2O_3 fillers and the PANI matrix.[49,52]

3.9. Mechanism exploration of surface initialized polymerization (SIP) approach

To better understand the SIP process and elaborate on the SIP mechanisms, the surface functionality of the Al_2O_3 nanostructures before and after surface treatment is explored through FT-IR.

The surface treated sample is prepared as follows: Al_2O_3 NPTs (0.373 g) are mixed with the PTSA/APS solution with a fixed ratio of 30 : 18 mmol in 200 ml deionized water, following by one-hour sonication in an ice-water bath. Then, the NPT is removed from the solution by centrifugation and washed three times with deionized water. Finally, the obtained solid sample is dried at 80 °C for 8 hours. Fig. 10 shows the spectra of the Al_2O_3 NPTs before and after the surface treatment. The new peaks presented in the range 950 cm^{-1} to 1600 cm^{-1} from the surface treated Al_2O_3 NPTs indicate that the APS and PTSA are successfully anchored on the surface of Al_2O_3 NPTs. The broad peak around 1437 cm^{-1} and the multi-peaks within the range of 1000–1200 cm^{-1} are attributed to the S–O, S=O symmetric and

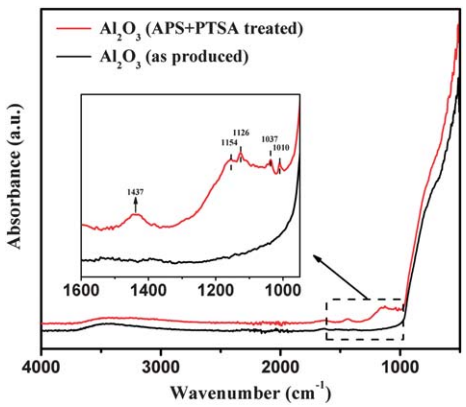

Fig. 10 FT-IR spectra of the Al_2O_3 NPTs before and after surface treatment with APS and PTSA.

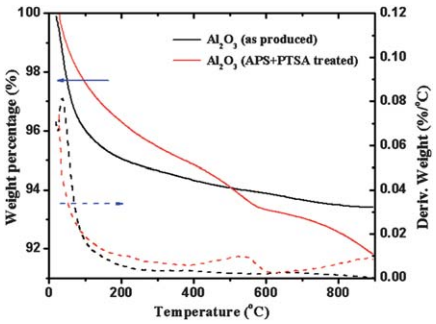

Fig. 11 The TGA curves of the Al_2O_3 NPTs before and after surface treatment with APS and PTSA.

Scheme 1 Mechanism of the nanocomposite fabrication by the SIP method.

asymmetric vibrations of APS and PTSA. This indicates that the oxidant (APS) and acid (PTSA) have been physicochemically attached on the surface of Al_2O_3 NPTs.

Fig. 11 shows the thermal degradation curve of the Al_2O_3 NPTs before and after the surface treatment. The Al_2O_3 NPTs before surface treatment show a sharp decrease in weight percentage below 200 °C, which corresponds to the elimination of moisture. And the weight loss curve is relatively stable afterward. The intense peak in DTG curve (dash line) at this area confirms the weight loss. After treating with APS and PTSA, the NPTs show an obvious weight loss starting around 400 °C besides the moisture removal below 200 °C. The broad peak centered at around 550 °C in DTG curve further confirms the weight loss, which is due to the decomposition of the APS and PTSA at elevated temperatures. Both FT-IR and TGA curves confirm the existence of APS and PTSA on the surface of Al_2O_3 NPTs, which is essentially important for initializing the polymerization starting from the surface of Al_2O_3 NPTs and explains the strong interfacial interaction between the polymer matrix and Al_2O_3 NPTs as evidenced by the TEM observation, Fig. 5. Scheme 1 illustrates the two steps for fabricating PNCs with SIP method.

4. Conclusions

Al_2O_3 nanostructures with different morphologies (*i.e.* nanofibers, nanoplatelets, nanorods and nanoflakes) are synthesized using hydrothermal procedures followed by a dehydration process. Their corresponding conductive polyaniline PNCs are successfully fabricated by a surface initialized polymerization method. The crystalline structure of PANI is affected by the "seeding" behavior of Al_2O_3 nanostructures and also depends on the morphology of the Al_2O_3 nanostructures. The electrical conductivity and dielectric permittivity of these PNCs are strongly related to the morphology and dispersion quality of the nanofillers. The temperature dependent resistivity of pure PANI and its PANI/Al_2O_3 PNCs depicts a quasi 3-d variable range

hopping (VRH) electron transportation mechanism. The extent of charge carrier delocalization calculated from VRH is well correlated to the dielectric response of these PNCs. The enhanced thermal stability of the PANI/Al_2O_3 PNCs as compared to pure PANI indicates a strong interaction between the polymer matrix and nanofillers as evidenced by DSC analysis. The two-step mechanism of the SIP method is proposed based on the surface functionality before and after surface treatment of the Al_2O_3 nanostructures as analyzed by FT-IR and TGA.

Acknowledgements

This project is supported by the National Science Foundation-Nanoscale Interdisciplinary Research Team and Materials Processing and Manufacturing (CMMI-1030755). Partial financial support from Northrop Grumman Corporation is acknowledged. D. P. Young acknowledges support from the NSF under Grant No. DMR 04-49022.

References

1 P. Podsiadlo, A. K. Kaushik, E. M. Arruda, A. M. Waas, B. S. Shim, J. Xu, H. Nandivada, B. G. Pumplin, J. Lahann, A. Ramamoorthy and N. A. Kotov, *Science*, 2007, **318**, 80–83.
2 P. Podsiadlo, Z. Liu, D. Paterson, P. B. Messersmith and N. A. Kotov, *Adv. Mater.*, 2007, **19**, 949–955.
3 J. Zhu, S. Wei, X. Chen, A. B. Karki, D. Rutman, D. P. Young and Z. Guo, *J. Phys. Chem. C*, 2010, **114**, 8844–8850.
4 X. Chen, S. Wei, C. Gunesoglu, J. Zhu, C. S. Southworth, L. Sun, A. B. Karki, D. P. Young and Z. Guo, *Macromol. Chem. Phys.*, 2010, **211**, 1775–1783.
5 Z. Guo, S. E. Lee, H. Kim, S. Park, H. T. Hahn, A. B. Karki and D. P. Young, *Acta Mater.*, 2009, **57**, 267–277.
6 Z. Guo, S. Park, H. T. Hahn, S. Wei, M. Moldovan, A. B. Karki and D. P. Young, *J. Appl. Phys.*, 2007, **101**, 09M511.
7 J. Zhu, S. Wei, J. Ryu, M. Budhathoki, G. Liang and Z. Guo, *J. Mater. Chem.*, 2010, **20**, 4937–4948.
8 J. Zhu, S. Wei, J. Ryu, L. Sun, Z. Luo and Z. Guo, *ACS Appl. Mater. Interfaces*, 2010, **2**, 2100–2107.
9 Z. Guo, H. T. Hahn, H. Lin, A. B. Karki and D. P. Young, *J. Appl. Phys.*, 2008, **104**, 014314.
10 S. Liu, L. Wei, L. Hao, N. Fang, M. W. Chang, R. Xu, Y. Yang and Y. Chen, *ACS Nano*, 2009, **3**, 3891–3902.
11 Y. Xia, P. Yang, Y. Sun, Y. Wu, B. Mayers, B. Gates, Y. Yin, F. Kim and H. Yan, *Adv. Mater.*, 2003, **15**, 353–389.
12 L.-S. Li, J. Hu, W. Yang and A. P. Alivisatos, *Nano Lett.*, 2001, **1**, 349–351.
13 B. O. Dabbousi, J. Rodriguez-Viejo, F. V. Mikulec, J. R. Heine, H. Mattoussi, R. Ober, K. F. Jensen and M. G. Bawendi, *J. Phys. Chem. B*, 1997, **101**, 9463–9475.
14 Y. Mao and S. S. Wong, *J. Am. Chem. Soc.*, 2006, **128**, 8217–8226.
15 J. Wang, E. Khoo, P. S. Lee and J. Ma, *J. Phys. Chem. C*, 2008, **112**, 14306–14312.
16 W. Cheng, E. Baudrin, B. Dunn and J. I. Zink, *J. Mater. Chem.*, 2001, **11**, 92–97.
17 L. Wang, A. Teleki, S. E. Pratsinis and P. I. Gouma, *Chem. Mater.*, 2008, **20**, 4794–4796.
18 G. Wang, Y. Ji, X. Huang, X. Yang, P.-I. Gouma and M. Dudley, *J. Phys. Chem. B*, 2006, **110**, 23777–23782.
19 X.-L. Li, T.-J. Lou, X.-M. Sun and Y.-D. Li, *Inorg. Chem.*, 2004, **43**, 5442–5449.
20 J. Zhu, S. Wei, L. Zhang, Y. Mao, J. Ryu, P. Mavinakuli, A. B. Karki, D. P. Young and Z. Guo, *J. Phys. Chem. C*, 2010, **114**, 16335–16342.
21 J. Zhu, S. Wei, L. Zhang, Y. Mao, J. Ryu, A. B. Karki, D. P. Younge and Z. Guo, *J. Mater. Chem.*, 2011, **21**, 342–348.
22 A. G. MacDiarmid, *Synth. Met.*, 1997, **84**, 27–34.
23 J. Huang, S. Virji, B. H. Weiller and R. B. Kaner, *J. Am. Chem. Soc.*, 2002, **125**, 314–315.
24 D. Mishra, S. Anand, R. K. Panda and R. P. Das, *Mater. Lett.*, 2000, **42**, 38–45.
25 C. Nédez, J.-P. Boitiaux, C. J. Cameron and B. Didillon, *Langmuir*, 1996, **12**, 3927–3931.
26 A. Laachachi, M. Cochez, E. Leroy, P. Gaudon, M. Ferriol and J. M. L. Cuesta, *Polym. Adv. Technol.*, 2006, **17**, 327–334.
27 Z. Guo, P. Tony, C. Oyoung, Y. Wang and H. T. Hahn, *J. Mater. Chem.*, 2006, **16**, 2800–2808.
28 J. Yang, R. L. Frost and Y. Yuan, *Thermochim. Acta*, 2009, **483**, 29–35.
29 N. Lepot, M. K. Van Bael, H. Van den Rul, J. D'Haen, R. Peeters, D. Franco and J. Mullens, *Ceram. Int.*, 2008, **34**, 1971–1974.
30 X. Y. Chen, Z. J. Zhang, X. L. Li and S. W. Lee, *Solid State Commun.*, 2008, **145**, 368–373.
31 X.-R. Zeng and T.-M. Ko, *J. Polym. Sci., Part B: Polym. Phys.*, 1997, **35**, 1993–2001.
32 S. Quillard, G. Louam, J. P. Buisson, M. Boyer, M. Lapkowski, A. Pron and S. Lefrant, *Synth. Met.*, 1997, **84**, 805–806.
33 P. Pernice, S. Esposito, A. Aronne and V. N. Sigaev, *J. Non-Cryst. Solids*, 1999, **258**, 1–10.
34 J. P. Pouget, M. E. Jozefowicz, A. J. Epstein, X. Tang and A. G. MacDiarmid, *Macromolecules*, 1991, **24**, 779–789.
35 J. B. M. Krishna, A. Saha, G. S. Okram, A. Soni, S. Purakayastha and B. Ghosh, *J. Phys. D: Appl. Phys.*, 2009, **42**, 095404.
36 G. iri-Marjanovi, L. Dragievi, M. Mojovi, S. Mentus, B. Dojinovi, B. marjanovi and J. Stejskal, *J. Phys. Chem. B*, 2009, **113**, 7116–7127.
37 X. Zhang and S. K. Manohar, *J. Am. Chem. Soc.*, 2004, **126**, 12714–12715.
38 A. Kassiba, W. Bednarski, A. Pud, N. Errien, M. Makowska-Janusik, L. Laskowski, M. Tabellout, S. Kodjikian, K. Fatyeyeva, N. Ogurtsov and Y. Noskov, *J. Phys. Chem. C*, 2007, **111**, 11544–11551.
39 P. Mavinakuli, S. Wei, Q. Wang, A. B. Karki, S. Dhage, Z. Wang, D. P. Young and Z. Guo, *J. Phys. Chem. C*, 2010, **114**, 3874–3882.
40 S. Chakrabarti, D. Banerjee and R. Bhattacharyya, *J. Phys. Chem. B*, 2002, **106**, 3061–3064.
41 Z. Guo, K. Shin, A. B. Karki, D. P. Young, R. B. Kaner and H. T. Hahn, *J. Nanopart. Res.*, 2009, **11**, 1441–1452.
42 R. Gangopadhyay, A. De and S. Das, *J. Appl. Phys.*, 2000, **87**, 2363–2367.
43 R. Tamura, E. Lim, T. Manaka and M. Wamoto, *J. Appl. Phys.*, 2006, **100**, 114515.
44 J. K. Nelson and C. J. Fothergill, *Nanotechnology*, 2004, **15**, 586–595.
45 D. Lee and K. Char, *Polym. Degrad. Stab.*, 2002, **75**, 555–560.
46 D. Lee, K. Char, S. W. Lee and Y. W. Park, *J. Mater. Chem.*, 2003, **13**, 2942–2947.
47 P. K. Khanna, N. Singh, S. Charan and A. K. Viswanath, *Mater. Chem. Phys.*, 2005, **92**, 214–219.
48 J. Deng, C. He, Y. Peng, J. Wang, X. Long, P. Li and A. S. C. Chan, *Synth. Met.*, 2003, **139**, 295–301.
49 J. Yang, C. Wang, K. Wang, Q. Zhang, F. Chen, R. Du and Q. Fu, *Macromolecules*, 2009, **42**, 7016–7023.
50 A. R. Bhattacharyya, T. V. Sreekumar, T. Liu, S. Kumar, L. M. Ericson, R. H. Hauge and R. E. Smalley, *Polymer*, 2003, **44**, 2373–2377.
51 J. A. Conklin, S.-C. Huang, S.-M. Huang, T. Wen and R. B. Kaner, *Macromolecules*, 1995, **28**, 6522–6527.
52 Z. H. Mbhele, M. G. Salemane, C. G. C. E. van Sittert, J. M. Nedeljković, V. Djoković and A. S. Luyt, *Chem. Mater.*, 2003, **15**, 5019–5024.